Comptes Rendus

Mécanique

Landry Giraud, Cédric Pouvreau, François Josse, William Berckmans, Fabien Lefebvre, Christophe Carrillo and Eric Feulvarch

A multi-phase linear kinematic elastoplastic model for the HAZ of welded S355J2 steel under low-cycle fatigue

CENTRE
MERSENNE

A multi-phase linear kinematic elastoplastic model for the HAZ of welded S355J2 steel under low-cycle fatigue

Landry Giraud [a, b]**, Cédric Pouvreau** [c]**, François Josse** [a]**, William Berckmans** [c]**, Fabien Lefebvre** [d]**, Christophe Carrillo** [e] **and Eric Feulvarch**[*, a]

[a] Univ Lyon, ENISE, LTDS UMR 5513 CNRS, 58 rue Jean Parot, 42023 Saint-Etienne cedex 02, France

[b] TRA-C industrie, ZAC les Olmes, 69490 Vindry-sur-Turdine, France

[c] Univ Bretagne Sud, IRDL UMR 6612 CNRS, Centre de Recherche, Rue de St Maude, 56100 Lorient, France

[d] CETIM, 52 Avenue Felix Louat, 60300 Senlis, France

[e] Haulotte Group, 27 rue d'Onzion, 42152 L'Horme, France

E-mails: l.giraud@tra-c.com (L. Giraud), cedric.pouvreau@univ-ubs.fr (C. Pouvreau), francois.josse@enise.fr (F. Josse), william.berckmans@univ-ubs.fr (W. Berckmans), Fabien.Lefebvre@cetim.fr (F. Lefebvre), ccarrillo@haulotte.com (C. Carrillo), eric.feulvarch@enise.fr (E. Feulvarch)

Abstract. The aim of this paper is to develop a linear kinematic elastoplastic model for simulating the mechanical behavior of a heat-affected zone under low-cycle fatigue for welded S355J2 low-carbon steel. First, an experimental procedure is developed by means of a Gleeble machine for creating macroscopic tensile specimens with different homogeneous metallurgical compositions according to a welding continuous cooling transformation diagram. Then, cyclic tensile tests are carried out by prescribing different strain amplitudes up to 1%. By considering the stabilized behavior at mid-life, the yield stress and hardening modulus are identified as functions of the metallurgical composition by means of a linear mixture rule. Comparisons with numerical simulations are presented to show the efficiency of the multi-phase cyclic linear kinematic elastoplastic model proposed in this work.

Keywords. Gleeble, Weld, HAZ, Low-cycle fatigue, Kinematic hardening.

Manuscript received 3rd May 2020, revised 17th June 2020, accepted 16th July 2020.

1. Introduction

The welding process is an assembling technique extensively used in many domains such as the naval industry, nuclear engineering, and the oil industry since the early twentieth century. Unfortunately, fusion welding processes can have a detrimental influence on the low-cycle-fatigue life of welded structures. In the case of 18% Cr ferritic stainless steel, Benoit *et al.* [1]

---

[*] Corresponding author.

investigated experimentally the mechanical behavior of a welded joint by means of strain-controlled tests. Rettenmeier *et al.* [2] studied the fatigue lifetime of a multi-axially loaded crane runway structure made of welded S355J2 steel. Baptista *et al.* [3] analyzed the fatigue behavior of welded railway rails. All these studies are highly linked to the welding parameters used because the microstructure and therefore the mechanical response will be different if the welding configuration changes.

In the case of low-carbon steel, fusion welding produces weakening zones often located in the heat-affected zone (HAZ) on each side of the joint. The HAZ is a zone where the parent metal microstructure is affected by thermal history. Solid state metallurgical transformations occur in this area, which leads to a gradient of mechanical properties. For simulating the influence of the welding parameters on the low-cycle-fatigue lifetime, it is thus necessary to compute the phase distribution in the HAZ and to integrate its influence into the cyclic behavior for assessing the stabilized mechanical state of a structure. To date, the simulation of welding has been widely used [4]. However, there exists no multi-phase elastoplastic law for the HAZ of welded S355J2 steel.

To characterize the mechanical behavior, the first approach consists in carrying out heat treatments for creating homogeneous macroscopic tensile specimens. Eggeler *et al.* [5] applied this approach to characterize the creep behavior of welded P91 steel. A similar heat treatment technique was applied by Sorkhabi and Vakili-Tahami [6] for welded 304L stainless steel. Unfortunately, such an approach does not simulate the cooling and heating rates induced by a welding operation. Thus, heat treatments are not appropriate for studying welded HAZs in the case of steel with phase changes. Regardless of phase proportions, the cooling and heating rates can also have an impact on the grain size and the type of microstructure.

Thermal–mechanical simulators can also be used to simulate the HAZ of a welded joint. The advantage of these devices is the regulation of the heating and cooling rates by means of thermocouples placed on the specimens studied. This technique allows simulating a specific microstructure as described by Kim *et al.* [7], who obtained a coarse-grained HAZ and a fine-grained HAZ for welded HSB800 steel. In this way, Wang *et al.* [8] studied the influence of the cooling rate on the toughness of bainite E550 grade offshore engineering steel. Hu *et al.* [9] used a similar method to characterize the toughness of V–N high-strength steel. Shao *et al.* [10] investigated the influence of the continuous cooling rate on the mechanical and microstructural behavior of Ti–22Al–Nb. Liu *et al.* [11] carried out Gleeble simulations by means of temperatures determined by a high-temperature infrared thermometer during a tungsten inert gas welding operation. The microstructural analysis showed the influence of the maximal temperature on the carbide behavior in a welded joint.

The aim of this paper is to develop a linear kinematic elastoplastic model to simulate the mechanical behavior of an HAZ under low-cycle fatigue for welded S355J2 low-carbon steel. In the first part of this paper, an experimental procedure is developed by means of a Gleeble machine so as to create macroscopic tensile specimens having a controlled metallurgical phase composition according to a welding continuous cooling transformation (CCT) diagram. In the second part, the specimen production is analyzed, with particular emphasis on the assessment of reproducible thermal cycles. The phase compositions are characterized in different ways for each form of the thermal kinetics: microstructural observation, phase volume determination, and microhardness. In the third and last part, cyclic tensile tests are carried out by prescribing different strain amplitudes up to 1%. By considering the stabilized behavior at mid-life, the yield stress and the hardening modulus are identified as functions of the metallurgical composition by means of a linear mixture rule. Comparisons with numerical simulations are presented to show the efficiency of the new multi-phase cyclic linear kinematic elastoplastic model.
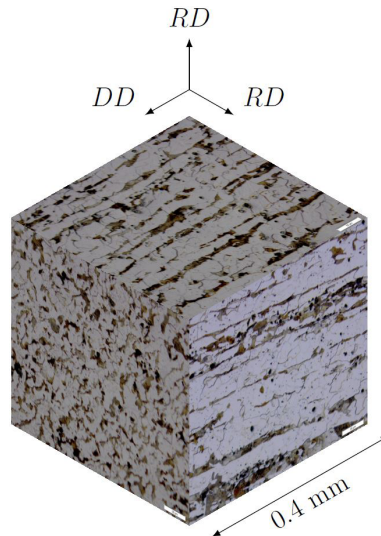
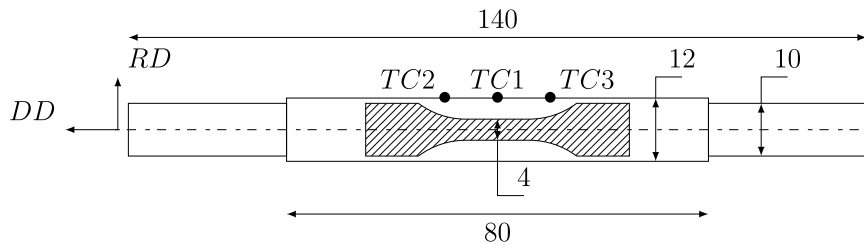**Figure 1.** Pseudo-3D optical micrographs of cold-drawn S355J2.

Figure 2. Geometry of the specimen for the Gleeble treatment (mm).

2. Experimental procedure

2.1. *Material*

The S355J2 material is low-carbon steel subjected to phase changes. In this case, the material studied has been produced by cold drawing, and it attains 184 HV_{30} hardness with a ferrito-pearlitic structure shown in Figure 1. Ferrite is associated with pearlite, which is composed of cementite (carbon) and ferrite itself. Pearlite can be identified in Figure 1 by the dark stripes according to the cold drawing direction (*DD*) of the material.

2.2. *Specimens*

Heat treatment was performed using a Gleeble 3500 thermomechanical simulator from DSI Inc. The geometry of the specimens is presented in Figure 2. The specimens have a cylindrical gauge zone with a diameter equal to 12 mm and a gauge length of 80 mm. Both extremities are reduced to a 10 mm diameter to fit the Gleeble clamps. The final cyclic tensile specimens (hatched area) are reduced to a 4 mm diameter with a 12 mm gauge length as shown in Figure 3.

The specimen is mounted between copper wedge clamps, and it is tightened by a torque wrench to ensure procedure repeatability. The cylindrical quenching system is visible up and
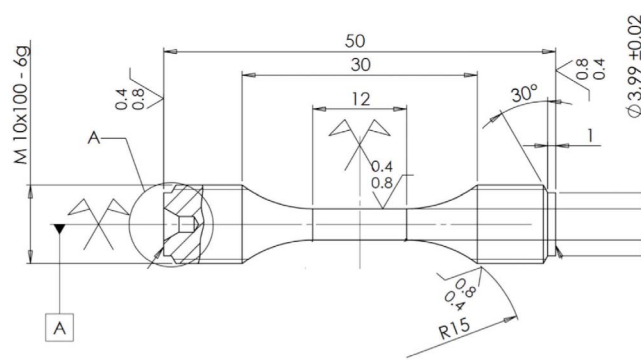
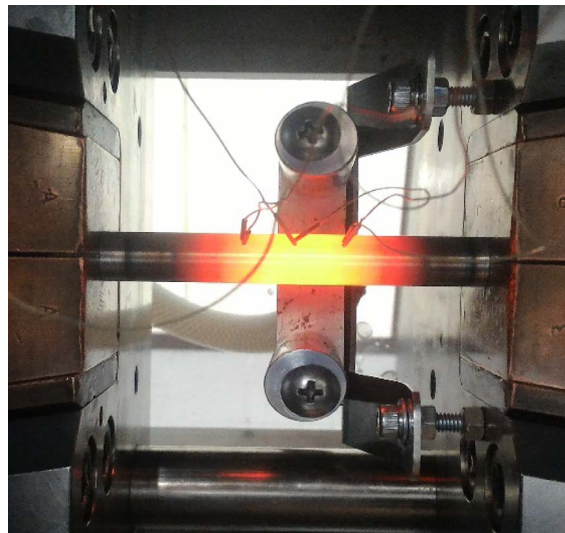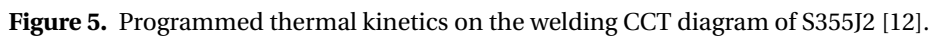**Figure 3.** Final geometry of the tensile specimen (mm).

Figure 4. Setup of the specimen during experiments.

down the sample. As can be seen in the photograph (Figure 4), there is a temperature gradient along the longitudinal axis of the sample. To control and monitor the temperature of the sample, three K-type thermocouples (*TCx* in Figure 2) are flash-welded to the surface. *TC1* is placed at the center of the specimen, and it is used as the control thermocouple by the Gleeble machine to follow up the imposed thermal kinetics. *TC2* and *TC3* are located at 5 mm on both sides of *TC1*. They are used to monitor the homogeneity of thermal treatment along the longitudinal axis.

2.3. *Gleeble simulation of thermal kinetics*

Four target metallurgical phase compositions were initially defined from the CCT diagram presented in Figure 5. For each composition, nine samples were produced. The programmed thermal cycles comprise three phases: heating, austenitization, and cooling.

The heating and austenitization phases are common to all cycles. During these phases, the temperature rises to 900 °C (above Ac3) at a heating rate of 100 °C·s^{-1}. The temperature is then maintained for 60 s to ensure complete austenitization of the specimen in the gauge zone.

Figure 5. Programmed thermal kinetics on the welding CCT diagram of S355J2 [12].

The programmed cooling kinetics for different thermal cycles are reported in Figure 5. To avoid the ferritic transformation zone and ensure the whole bainitic transformation (*B* specimens; blue curve in Figure 5), an isothermal transformation process is preferred to a CCT. The samples are quenched from 900 °C to 500 °C using helium at a pressure of 200 kPa. The temperature is then maintained at 500 °C for 1000 s before carrying out a second helium quenching operation down to room temperature (see Figure 6(a)).

The first intermediate (*BM*1) specimens (green curve in Figure 5) are obtained by a two-step quenching operation. During the first step, the sample is cooled down to 400 °C using helium (pressure range 150 kPa–250 kPa) at a targeted cooling rate of 25 °C·s^{-1} derived from the original CCT diagram. The second step is water quenching down to room temperature to ensure proper martensite formation (see Figure 6(b)).

The second intermediate (*BM*2) specimens (red curve in Figure 5) are also obtained by means of a two-step quenching operation. The helium quenching pressure is held constant (250 kPa) due to the short transformation time (approximately 2 s) according to the CCT diagram. In contrast to the previous samples, following a cooling rate of 75 °C·s^{-1} is difficult. Indeed, we will show that we have a nonconstant cooling rate below the targeted cooling rate. To compensate for this lack of cooling rate, the second quenching step is anticipated at 475 °C (see Figure 6(c)).

To produce (*M*) specimens (100% of martensite; orange curve in Figure 5), the sample design imposes water quenching (<20 °C, 400 kPa) to achieve cooling rates above 90 °C·s^{-1}. However, in this case, the precise control of cooling kinetics is impossible.

2.4. *Microstructure characterization methods*

Samples were extracted from the specimens to perform microstructural observations. The samples were polished down to 1 μm (automatic machine TegraPol-31, Struers) and finally etched in a 4% nitric acid and ethanol solution to reveal the microstructure.

Observations were made using an optical microscope (AX70 Provis, Olympus), and phase volume fractions were determined by the ASTM procedure [13].

Microhardness measurements were performed using a Mitutoyo AVK-C2 device with a Vickers indenter under a 30 kgf load. The load was chosen to be comparable with the data available in the literature.
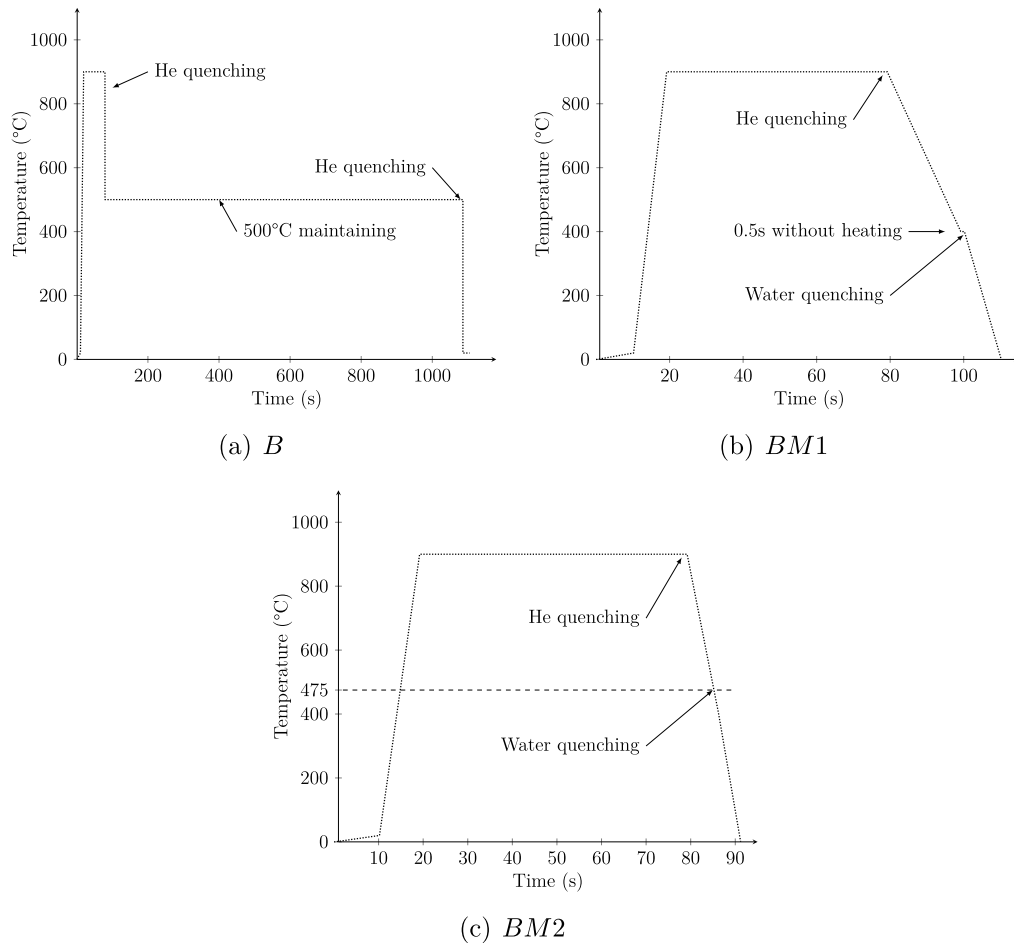
(a) B (b) $BM1$

(c) $BM2$

Figure 6. Cooling kinetics programmed on the Gleeble simulator.

2.5. *Cyclic tensile tests*

All cyclic tests were carried out on a traction–compression machine with an MTS brand extensometer. The evolution over time of the prescribed strain followed a triangular signal with a frequency of 1 Hz. The experiments were conducted at a loading ratio R equal to -1.

3. Analysis of Gleeble simulations

In this section, the homogeneity and the reproducibility of the metallurgical phase composition are examined by analyzing experimental thermal kinetics. Moreover, the phase composition of the different samples is assessed through metallographic observations and hardness measurements.

3.1. *Thermal analysis*

3.1.1. *Thermal response of specimens*

Figure 7 shows the typical recorded temperatures (one sample out of nine samples for each metallurgical composition). First, it is interesting to observe the satisfactory agreement with
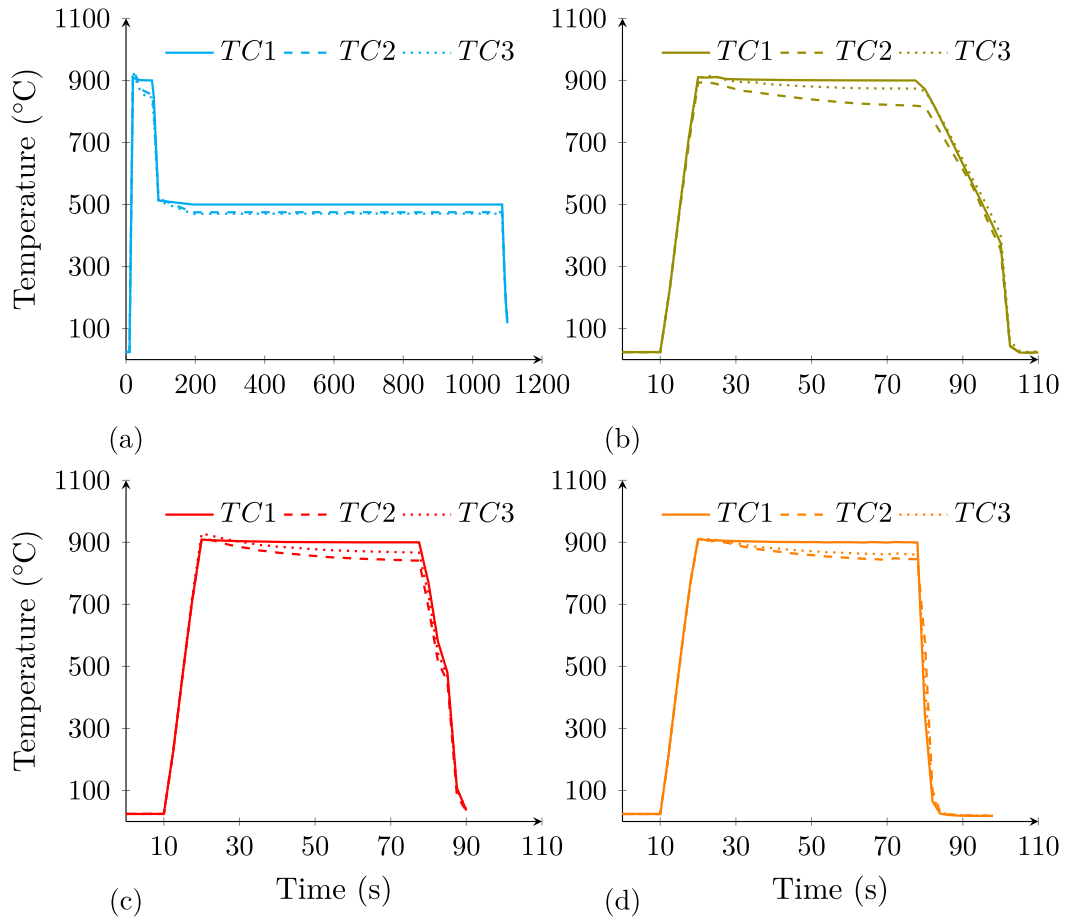
Figure 7. Typical thermal kinetics of (a) *B*, (b) *BM*1, (c) *BM*2, and (d) *M*.

the programmed thermal cycles previously described for the four cases. As can be seen in the four plots, the temperature is maintained above AC3 at approximately 900 °C during the austenitization phase for *TC1*. During this phase, the recorded temperatures *TC*2 and *TC*3 show a slight decrease, but they still remain above AC3 (867 °C). During the quenching phase, there are slight differences among *TC*2, *TC*3, and *TC*1. These are the results of a slight difference in thermal conduction between the two clamps and a small asymmetry of the quenching system. Despite the above observations, the temperature measurements on the surface ensure that austenitization is achieved in the zone located between *TC2* and *TC3*, especially inside the volume corresponding to the zone of the tensile specimens.

3.1.2. *Thermal cycle homogeneity and reproducibility*

Because of the high dependence on the cooling rates of microstructural transformations, a simple study of temperature evolution is not sufficient to analyze the repeatability and homogeneity of the samples. For the three continuous cooling treatments (*M*, *BM*1, and *BM*2), a study of the cooling rate is carried out in the transformation zone. For the isothermal treatment *B*, only a discussion of the temperature in the bainitic zone is conducted. Figures 8(a), 8(b), and 8(c) show the evolution of the average cooling rate as a function of temperature. The average cooling rates
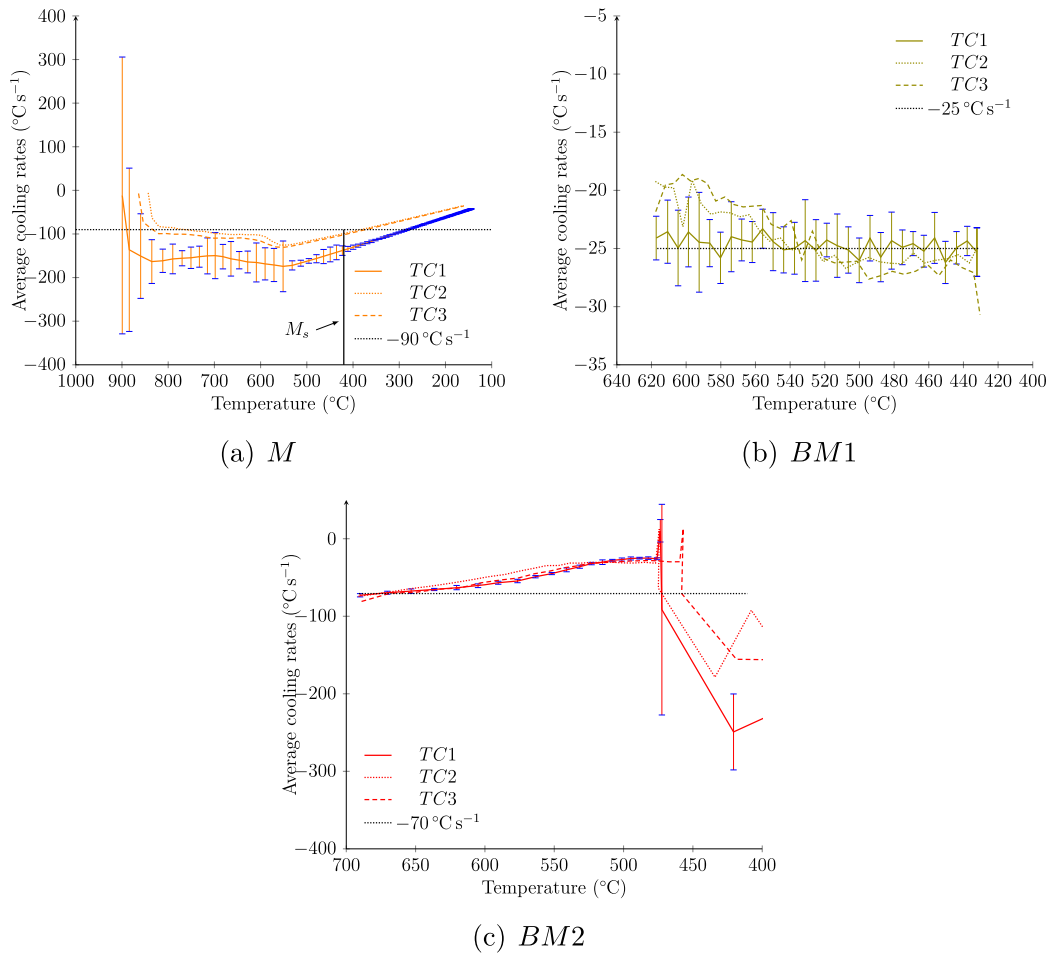
(a) M

(b) $BM1$

(c) $BM2$

Figure 8. Thermal kinetics as a function of temperature.

for the three thermocouples are calculated by considering the nine samples for each composition. The standard deviations are plotted only for *TC1* for convenience.

Regarding the (*M*) composition (see Figure 8(a)), an analysis of the whole treatment is carried out. In the first part of the cooling stage, we can note the stability of the cooling rate (typically $-150\,°C·s^{-1}$ up to 550 °C). The three average cooling rate values are below the limit of $-90\,°C·s^{-1}$ up to the M_s temperature. Therefore, the cooling rates are always sufficient to avoid the bainitic transformation zone. Moreover, one can note that the standard deviation of *TC1* near M_s is approximately $\pm10\,°C·s^{-1}$. All these observations make it possible to conclude satisfactory homogeneity of the cooling rate in the zone of the tensile specimen.

For the (*BM*1) composition in Figure 8(b), one can note that on the whole transformation zone (from 620 °C to 430 °C), the expected cooling rate is attained at *TC1*. As far as *TC2* and *TC3* are concerned, the cooling rates are slightly lower at the beginning of the transformation (from 620 °C to 540 °C) and then slightly higher at the end (from 540 °C to 430 °C). The difference between the three thermocouples is very small and is included in the standard deviation ($\pm1.0\,°C·s^{-1}$ to $\pm4.3\,°C·s^{-1}$) of *TC1* for the major part of the transformation zone, thereby inducing satisfactory homogeneity and repeatability of the thermal history.
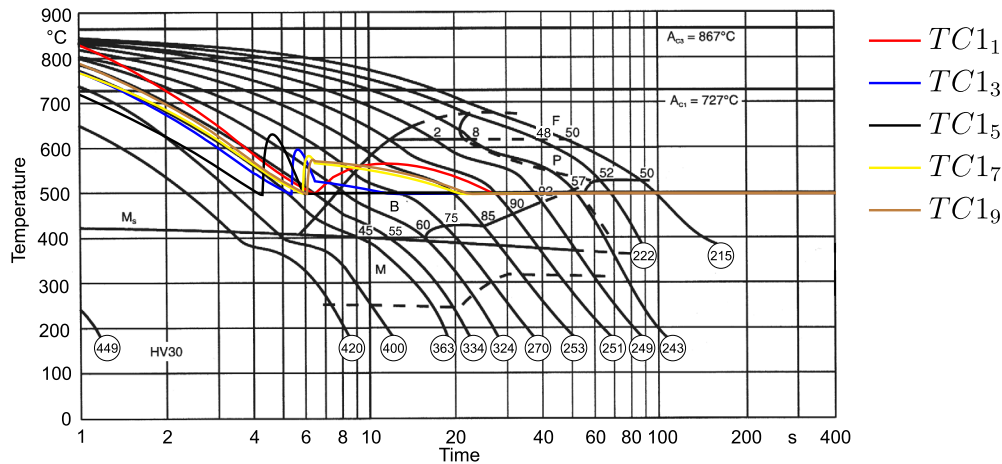
Figure 9. Thermal kinetics in the case of 100% bainite (*B*).

As regards the (*BM*2) composition (see Figure 8(c)), the targeted cooling rate is difficult to follow because of the high transformation speed. The experimental kinetics are slower than the targeted kinetics. To avoid too high a proportion of bainite, the second quenching step has been anticipated. One can note that the difference among the three thermocouples is approximately 10 °C. This demonstrates satisfactory homogeneity. Moreover, the standard deviation is equal to $\pm 1.3\,°\text{C}\cdot\text{s}^{-1}$, thereby inducing good repeatability during the transformation zone.

For the isothermal transformation required to obtain the (*B*) composition, only the evolution of the temperature over time is analyzed. Figure 9 shows, for convenience, five of the nine thermal forms of kinetics of *TC1* plotted all over the CCT diagram. A temperature rebound appears at the end of the quenching step before the temperature is held constant at 500 °C. The sudden change in temperature dynamics makes it difficult for the regulation system to maintain a constant temperature instantaneously. As the temperature always remains within the bainitic transformation zone and as the duration of the rebound is short, we infer that this phenomenon does not significantly affect the final phase composition. In this way, no effort has been made to minimize the temperature peak.

3.2. *Microstructural analysis*

Additionally, the work proposed focuses on the experimental analysis of the microstructure obtained by the Gleeble heat treatments.

3.2.1. *Micrograph analysis*

The different microstructures obtained are presented in Figure 10.

In Figure 10(a), an example of bainitic microstructure is presented. It is called granular bainite and is composed of ferrite grains in gray and cementite in black surrounding the ferrite grains. The martensite appears on the micrograph as black needles as shown in Figure 10(d). The microscopic observations confirm the formation of just a bainitic microstructure for the test *B* only as well as the formation of a full martensitic microstructure for test *M*. The tests *BM*1 and *BM*2 show respectively a mixture of bainite and martensite, with a high volume of bainite (in gray) for the micrograph *BM*1 and a high volume of martensite (in black) for the micrograph *BM*2 (Figures 10(b) and 10(c)).
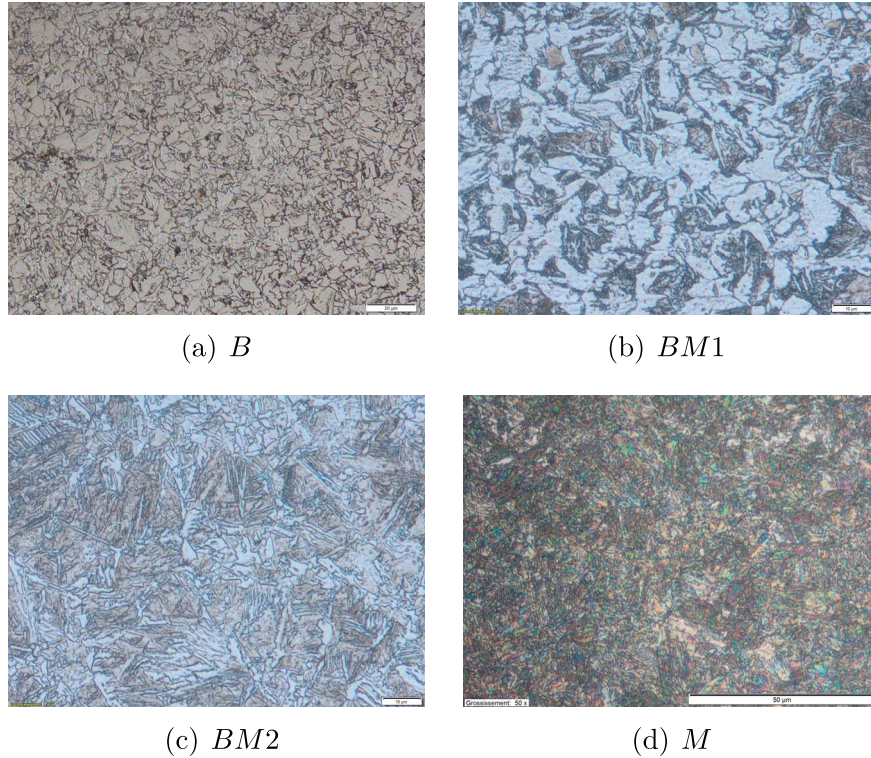
(a) B

(b) $BM1$

(c) $BM2$

(d) M

Figure 10. Micrographs of microstructures.

Table 1. Hardness measurements

Samples	B	$BM1$	$BM2$	M
Experimental microhardness (HV_{30})	233.6	287.3	371	442.8
Standard deviation	3.3	5.7	6.2	12.2

3.2.2. *Microhardness characterization*

Microhardness is measured on each sample along the radius to analyze the homogeneity between the surface and the center of the specimens. The average value and the standard deviation are estimated by means of 11 measurements summarized in Table 1. In Figure 11, the experimental values along the radius are reported to be compared to the closest values obtained from the CCT diagram of Figure 5 (dotted line). One can note that the microhardness values are quite homogeneous along the radius. For B and M, the observations fit quite well the targeted values. For $BM2$, the microhardness measurements are in good accordance with a phase proportion of bainite that would be equal to 25%. As far as $BM1$ is concerned, the experimental measurements are all greater than the microhardness corresponding to 75% of bainite (270 HV_{30}). Therefore, the proportion of bainite must be lower than 75% for $BM1$.

3.2.3. *Volume phase determination*

The specimens $BM1$ and $BM2$ composed of a mixture of bainite and martensite are analyzed to determine the volume of each metallurgical phase following the standard manual method E562-01 [13]. After an extraction of sections in the DD–RD plane, 18 ($BM1$) and 25 ($BM2$)
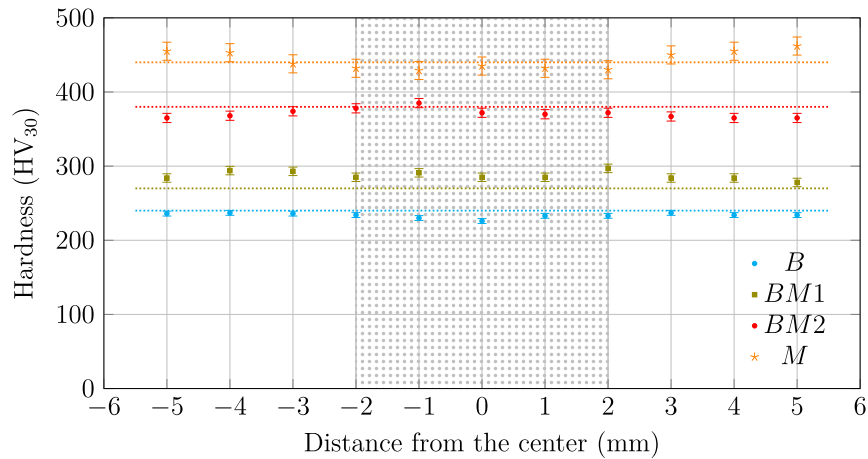
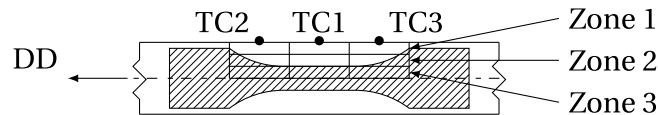**Figure 11.** Distribution of hardness from the axis of the sample.

Figure 12. Location of volume phase determination.

Table 2. Bainitic volume fractions as estimated by the E562-01 method

		$TC2$ (%)	$TC1$ (%)	$TC3$ (%)	$\bar{P}$ (%)	s (%)	CI 95% (%)	%RA (%)
$BM1$	Zone 1	67.6	75	68.8	65.7	5.9	2.9	4.5
	Zone 2	69.9	66.2	64.5				
	Zone 3	60.6	62.1	65.9				
$BM2$	Zone 1	22.5	22.4	19.3	25.2	5.9	2.5	9.8
	Zone 2	32.0	26.9	24.8				
	Zone 3	28.2	26.9	19.3				

micrographs (fields) are taken. To verify the homogeneity of the sections, the fields are located on each axial position of the thermocouples in three areas (top/middle/bottom) as described in Figure 12. A grid of 88 points with a spacing of 10 μm in both the x and y directions is then overlaid on micrographs. The number of fields and the grid size are chosen to ensure a 10% relative accuracy of the estimate of volume fraction as reported in the E562-01 standard. The fraction volumes are reported in Table 2. For $BM2$, the estimated volume fraction of bainite is in good agreement with the value of 25% from the CCT diagram in Figure 5. For $BM1$, the average estimated volume fraction $\bar{P}$ is approximately 65.7%. This observation supports the higher hardness measured above for this specimen.

For both specimens, the bainite volume fraction within the region of interest is quite homogeneous as indicated by the relatively low confidence intervals (CI 95%).

In both cases, the calculated relative accuracy of the estimated volume fraction (%RA) is better than the target of 10% established using the initial grid choice and the number of sections observed.

Table 3. Number of experiments for each value of the uniaxial strain amplitude ϵ_a

ϵ_a (%)	B	$BM1$	$BM2$	M
0.25	-	1	1	-
0.3	1	2	2	2
0.35	-	2	2	-
0.5	2	2	2	3
0.75	2	2	2	2
1	3	-	-	2

4. Multi-phase linear kinematic elastoplastic model

4.1. *Cyclic tensile tests*

All the cyclic experiments are carried out at a loading ratio $R = -1$. Table 3 details the values of the uniaxial strain amplitude $\epsilon_a = (\epsilon_{\max} - \epsilon_{\min})/2$, which have been prescribed for the tensile specimens.

4.2. *Modeling of cyclic behavior for each specimen*

In this section, the cyclic elastoplastic behavior of each phase composition is described by means of the Prager linear kinematic hardening [14]. One can note that the Chaboche nonlinear kinematic hardening [15] can be used by means of a superposition of several Armstrong–Frederick rules [16]. Even if this model is used for modeling cyclic behaviors [17], its main appeal is its ability to simulate a ratcheting effect [18] as do the Ohno–Wang model [19] and the Chen–Jiao–Kim model [20]. This means that the use of the Chaboche rule can produce an unrealistic ratcheting phenomenon if it is not correctly calibrated. In the case of a large industrial welded structure, this could happen even if it is subjected to a global loading ratio $R = -1$. Indeed, distortions for slender structures can lead to local ratios other than -1. Moreover, the local loadings can be non-radial because of the interactions between plastic and elastic zones and the coupling with welding residual stresses. The correct modeling of the ratcheting phenomenon requires cyclic tensile tests with a loading ratio R other than -1, which are not available in this study. Thus, the Prager rule has been chosen. The evolution of the kinematic tensorial variable $\mathbf{X}$ is collinear with the evolution of the plastic strain:

$$\mathbf{X} = \frac{2}{3} C \, \boldsymbol{\epsilon}^p, \tag{1}$$

where C and $\boldsymbol{\epsilon}^p$ denote the hardening modulus and the plastic strain tensor, respectively. The elastic domain is defined in a standard way as follows:

$$f = J_2(\boldsymbol{\sigma} - \mathbf{X}) - \sigma^y \leq 0, \tag{2}$$

where $\boldsymbol{\sigma}$ and J_2 are the stress tensor and the second invariant of the deviator, respectively.

For estimating the yield stress σ^y and C, stabilized cycles are extracted as a function of the uniaxial plastic strain (ϵ^p). By this method, the influence of the elastic strain on the estimation is avoided. For each metallurgical composition, the cyclic curves at mid-life are plotted on the same graph by refocusing each loop on the origin. As shown in Figure 13, a linear regression passing through the extrema allows estimating C and σ^y by means of the slope and the intersection with the vertical axis, respectively. The final parameters are taken equal to the average values of those from the positive (red in Figure 13) and negative (blue in Figure 13) extrema. Table 4 summarizes the final values obtained for the Prager linear kinematic hardening model for each metallurgical composition.
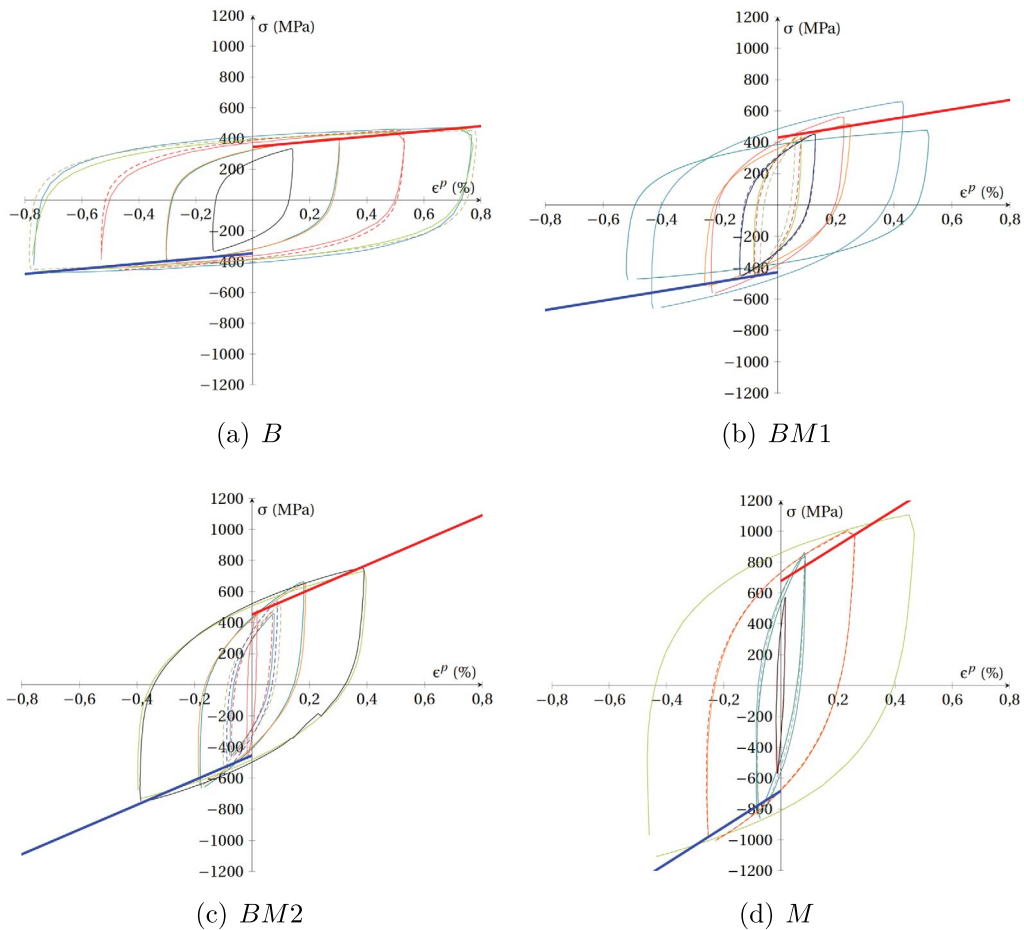
(a) B

(b) $BM1$

(c) $BM2$

(d) M

Figure 13. Estimation of the hardening modulus C and the yield stress σ^y.

Table 4. Values of C and σ^y for each metallurgical composition

	C (MPa)	σ^y (MPa)
B	16 762	345
$BM1$	30 117	429
$BM2$	79 683	453
M	117 170	680

4.3. *Identification of multi-phase linear kinematic elastoplastic model*

In this study, the influence of phase composition is assumed to be linear as proposed by Leblond *et al.* [21] for modeling strain hardening phenomena during phase transformations in steel. By this method, the parameters C and σ^y are defined by means of two linear functions depending on the phase proportion of bainite. Here, their expressions are determined from linear regressions plotted in Figure 14. As a verification, Figures 15 and 16 show the comparison between experiments and finite element method (FEM) simulations for $\epsilon_a = 0.3\%$ and $\epsilon_a = 0.75\%$. One can note that the computational results are very satisfactory.
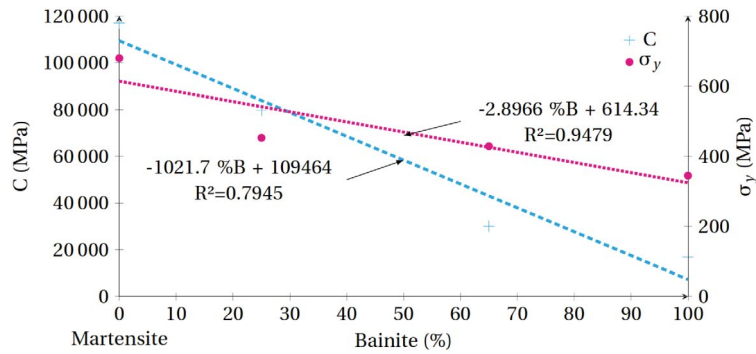
Figure 14. Evolutions of C and σ^y with the proportion of bainite.
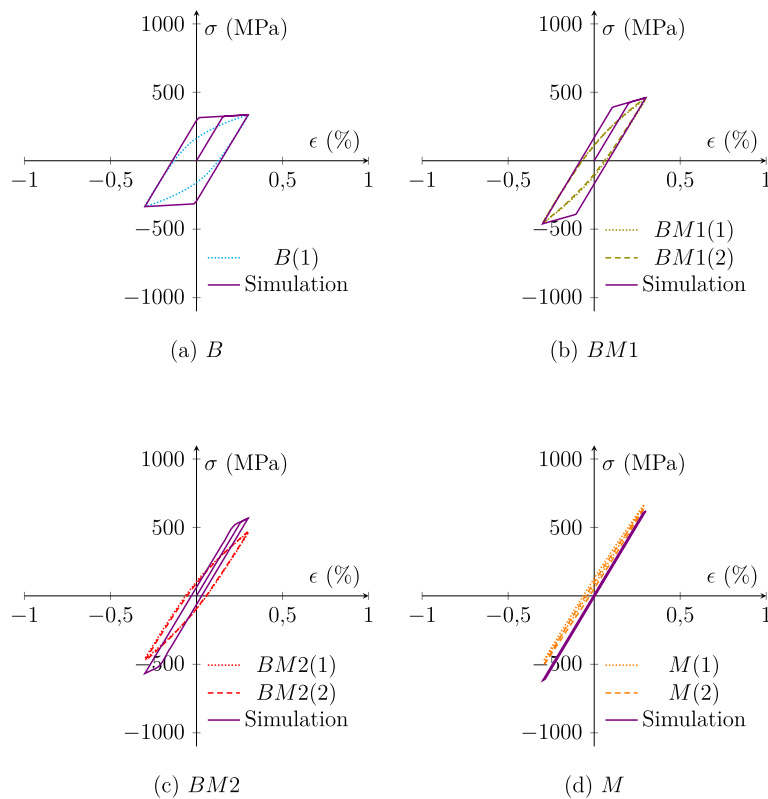

Figure 15. Comparisons between experiments (see Table 3) and the FEM simulation of cyclic tests for $\epsilon_a = 0.3\%$.

5. Conclusions

The goal of this paper is to develop a linear kinematic elastoplastic model for simulating the mechanical behavior of an HAZ under low-cycle fatigue for welded S355J2 low-carbon steel.

- Four specific imposed thermal kinetics are proposed to simulate metallurgical compositions according to an experimental welding CCT diagram.
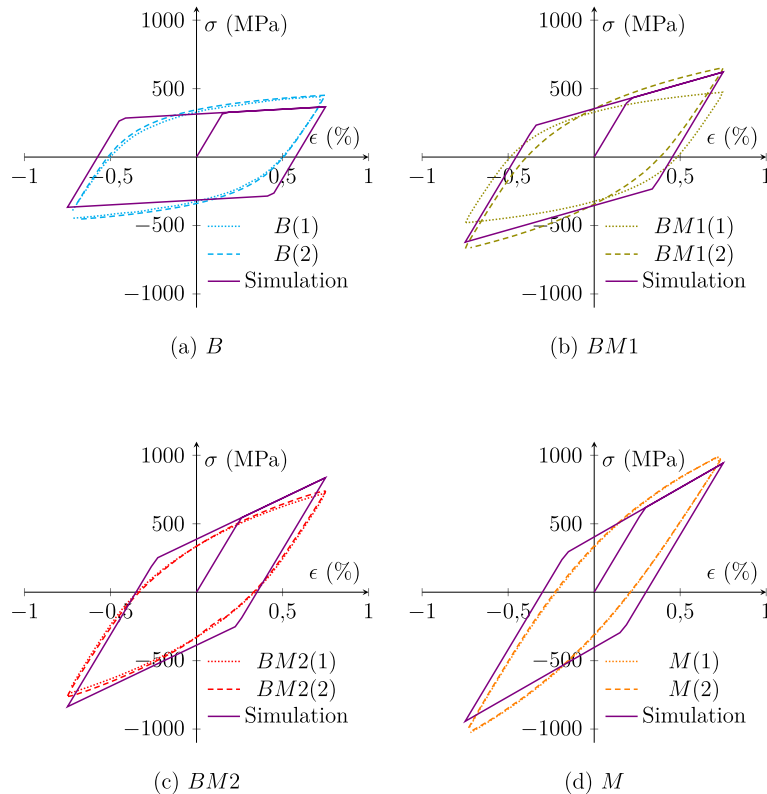
(a) B

(b) $BM1$

(c) $BM2$

(d) M

Figure 16. Comparisons between experiments (see Table 3) and the FEM simulation of cyclic tests for $\epsilon_a = 0.75\%$.

- An experimental procedure on a Gleeble machine is successfully developed to simulate specific thermal kinetics at high cooling rates.
- It is demonstrated that the resulting metallurgical compositions are obtained with very satisfactory homogeneity and repeatability.
- A linear kinematic hardening model is identified for each metallurgical composition comprising bainite and martensite.
- A multi-phase version of the Prager linear kinematic hardening is proposed by applying a linear mixture rule to phase proportions.

References

[1] A. Benoit, L. Remy, A. Koster, H. Maitournam, F. Roger, "Experimental investigation of the behavior and the low cycle fatigue life of a welded structure", *Mater. Sci. Eng. A* **595** (2014), p. 64-76.

[2] P. Rettenmeier, E. Roos, S. Weihe, "Fatigue analysis of multiaxially loaded crane runway structures including welding residual stress effects", *Int. J. Fatigue* **82** (2016), p. 179-187.

[3] R. Baptista, T. Santos, J. Marques, M. Guedes, V. Infante, "Fatigue behavior and microstructural characterization of a high strength steel for welded railway rails", *Int. J. Fatigue* **117** (2018), p. 1-8.

[4] E. Feulvarch, V. Robin, J. M. Bergheau, "Thermometallurgical and mechanical modelling of welding - application to multipass dissimilar metal girth welds", *Sci. Technol. Weld. Joining* **16** (2011), p. 221-231.

[5] G. Eggeler, A. Ramteke, M. Coleman, B. Chew, G. Peter, A. Burblies, J. Hald, C. Jefferey, J. Rantala, M. deWitte, "Analysis of creep in a welded P91 pressure vessel", *Int. J. Press. Vessels Pip.* **60** (1994), p. 237-257.

[6] A. H. D. Sorkhabi, F. Vakili-Tahami, "Experimental study of the creep behavior of parent, simulated HAZ and weld materials for cold-drawn 304l stainless steel", *Eng. Failure Anal.* **21** (2012), p. 78-90.

[7] S. Kim, D. Kang, T.-W. Kim, J. Lee, C. Lee, "Fatigue crack growth behavior of the simulated HAZ of 800mpa grade high-performance steel", *Mater. Sci. Eng. A* **528** (2011), p. 2331-2338.

[8] X. Wang, Z. Wang, X. Ma, S. Subramanian, Z. Xie, C. Shang, X. Li, "Analysis of impact toughness scatter in simulated coarse-grained HAZ of E550 grade offshore engineering steel from the aspect of crystallographic structure", *Mater. Charact.* **140** (2018), p. 312-319.

[9] J. Hu, L.-X. Du, J.-J. Wang, C.-R. Gao, "Effect of welding heat input on microstructures and toughness in simulated CGHAZ of V-N high strength steel", *Mater. Sci. Eng. A* **577** (2013), p. 161-168.

[10] L. Shao, S. Wu, S. Zhao, J. Ketkaew, H. Zhao, F. Ye, J. Schroers, "Evolution of microstructure and microhardness of the weld simulated heat-affected zone of Ti–22Al–25Nb (at.%) alloy with continuous cooling rate", *J. Alloys Compd.* **744** (2018), p. 487-492.

[11] W. Liu, F. Lu, R. Yang, X. Tang, H. Cui, "Gleeble simulation of the HAZ in Inconel 617 welding", *J. Mater. Process. Technol.* **225** (2015), p. 221-228.

[12] P. Seyffarth, B. Meyer, A. Scharff, *Großer Atlas Schweiß-ZTU-Schaubilder*, Deutscher Verlag für Schweißtechnik DVS-Verlag GmbH, 1992.

[13] "Standard Test Method for Determining Volume Fraction by Systematic Manual Point Count", ASTM E562-01, ASTM International, West Conshohocken, PA, 2001.

[14] W. Prager, "Recent developments in the mathematical theory of plasticity", *J. Appl. Phys.* **20** (1949), p. 235-241.

[15] L. Chaboche, "Time independent constitutives theories for cyclic plasticity", *Int. J. Plast.* **2** (1986), p. 149-188.

[16] P. J. Armstrong, C. O. Frederick, "A mathematical representation of the multiaxial Bauschinger effect, Berkeley Nuclear Laboratories, 1966", *Mat. High Temp.* **24** (2007), p. 11-26, Reprinted.

[17] J. B. Esnault, V. Doquet, P. Massin, "A three-dimensional analysis of fatigue crack paths in thin metallic sheets", *Int. J. Fatigue* **62** (2014), p. 119-132.

[18] A. H. Mahmoudi, H. Badnava, S. M. Pezeshki-Najafabadi, "An application of Chaboche model to predict uniaxial and multiaxial ratcheting", *Procedia Eng.* **10** (2011), p. 1924-1929.

[19] N. Ohno, D. Wang, "Kinematic hardening rules with critical state of dynamic recovery, Part I: formulation and basic features for ratchetting behavior", *Int. J. Plast.* **9** (1993), p. 375-390.

[20] X. Chen, R. Jiao, K. S. Kim, "On the Ohno Wang kinematic hardening rules of multiaxial", *Int. J. Plast.* (2005), p. 161-184.

[21] J. B. Leblond, J. Devaux, J. C. Devaux, "Mathematical modelling of transformation plasticity in steels, I: case of ideal-plastic phases, II: coupling with strain hardening phenomena", *Int. J. Plast.* **5** (1989), p. 551-591.